Acta Materialia 159 (2018) 309–319

Contents lists available at ScienceDirect

Acta Materialia

journal homepage: www.elsevier.com/locate/actamat

Full length article

Residual stress in polycrystalline alumina: Comparison of two-dimensional maps and integrated scans in fluorescence-based measurements

Chris A. Michaels, Robert F. Cook*

Materials Measurement Science Division, National Institute of Standards and Technology, Gaithersburg, MD, 20899, USA

ARTICLE INFO

Article history:
Received 17 April 2018
Received in revised form
9 August 2018
Accepted 14 August 2018
Available online 18 August 2018

Keywords:
Fluorescence
Stress and strain
Alumina (α-Al_2O_3)
Mapping
Image analysis

ABSTRACT

The spatially heterogeneous residual stress fields in a series of three polycrystalline alumina materials are compared using two fluorescence-based measurement techniques. In the first technique, 18 hyperspectral arrays of the Cr-based R_1 and R_2 ruby fluorescence line shifts are formed into two-dimensional maps of stress components, and experimental stress distributions are calculated using both spectral lines jointly. In the second technique, the data are formed into integrated scans reflecting the average spectra within the maps and assumed Gaussian stress distributions are calculated, using the spectral lines singly. Comparison of the distribution parameters shows that the single-peak-based integrated scan technique significantly overestimates the variation of the mean crystallographic stresses relative to the two-peak-based two-dimensional map technique. In addition, the integrated scan technique suggests standard deviations for the crystallographic stress distributions that are significantly greater than those determined from two-dimensional map observations. Although, when a sufficient area of the microstructure is examined, the averaged results of the two techniques agree, the two-dimensional map method is preferred as it makes full use of the two-peak spectra and provides explicit stress distribution determinations. For the approximately 15 μm grain size materials examined here the *c*-axis stress distributions determined from the mapping technique were characterized by means ± standard deviations of approximately (190 ± 40) MPa.

Published by Elsevier Ltd on behalf of Acta Materialia Inc.

1. Introduction

A residual stress state forms in dense polycrystalline alumina (Al_2O_3) on cooling from the sintering or processing temperature. The stress is due to the anisotropic coefficient of thermal expansion (CTE) of the constituent single-crystal Al_2O_3 grains [1]. If sufficiently large, such residual stresses can lead to spontaneous microcracking of a pristine material in the absence of an applied stress [2], and, in a cracked material under the influence of an applied stress, greatly affect the formation and action of microstructurally-based crack-wake fracture restraints [3]. Hence, residual stresses can greatly affect both the strength and toughness of polycrystalline Al_2O_3 and much work has thus focused on measuring and mapping residual stresses in Al_2O_3 microstructures. In particular, measurements of the shifts in the Cr related "ruby" R_1 and R_2 fluorescence lines in Al_2O_3 enable residual stresses to be measured (Cr is a ubiquitous substitutional impurity for Al in Al_2O_3): a brief review of stress measurement by fluorescence is given in Ref. [4] and an extensive review of the precision and accuracy of the stress-optical coefficients that form the basis for such measurements is given in Ref. [5]. The original work [6] that established fluorescence-based two-dimensional stress mapping in polycrystalline Al_2O_3 has been greatly extended by recent studies [4,7,8] that include multi-thousand-pixel images with sub-micrometer spatial resolution and sub-ten megapascal stress resolution of multiple stress components. However, prior works [9–12] have used a fluorescence-based integrated area approach to arrive at a stress measurement representing an average over a single, large, multi-micrometer scan. Both techniques—two-dimensional mapping and integrated scans—have advantages (see below), but a clear, quantitative comparison of the two methods is lacking. Such a comparison is required (1) to interpret prior results in terms of the new studies, and (2) to extend the ease of use of the

* Corresponding author.
E-mail addresses: chris.michaels@nist.gov (C.A. Michaels), robert.cook@nist.gov (R.F. Cook).

https://doi.org/10.1016/j.actamat.2018.08.025
1359-6454/Published by Elsevier Ltd on behalf of Acta Materialia Inc.

technique in establishing microstructure-residual stress relationships in polycrystalline Al_2O_3. A comparison is provided here using the set of materials that has been the subject of the recent works [4,7,8].

Fig. 1 is a schematic diagram that illustrates the methods and advantages of each stress measurement technique and how a comparison is made. In the *two-dimensional map* method, Fig. 1(a), the surface of a polycrystalline material, represented by the hexagonal pattern (of grain boundaries), is illuminated by a two-dimensional $M \times N$ array of sub-micrometer laser excitation spots, represented by the small gray discs. In practice, the two-dimensional array is generated by scanning the sample relative to the fixed, focused laser spot. The multiple optical fluorescence spectra, $I_{ij}(\nu)$, generated by the excitation are recorded for each spot, where I is intensity, ν is the energy of the fluorescent light, and i and j are spot indices. The resulting hyperspectral image is analyzed, concentrating on the R_1 and R_2 fluorescence peaks, including the peak intensities and peak positions at each spot, along with many other associated spectral fitting parameters; stresses are determined from the two peak positions at each spot. Two-dimensional maps are thus easily formed from pixels characterizing fluorescence or inferred stress quantities from the array of spots [4,7,8]. In the *integrated scan* method, Fig. 1(b), the surface of the polycrystalline material, again represented by a hexagonal pattern, is illuminated by a single, multi-micrometer laser probe represented by the large disc of area A. The single optical fluorescence spectrum, $I_A(\nu)$, generated by the excitation is recorded and analyzed for the R_1 and R_2 peaks, although typically only one peak is used: attention is focused on the single peak position and width to arrive at an effective Gaussian stress distribution within the probed area [9,10] (Note that Fig. 1 is not drawn to scale. In recent two-dimensional map experiments [4,7,8], the array spacing and spot size were both sub-μm and the Al_2O_3 grain size was about 15 μm or larger. In previous integrated scan experiments [9–12] the single spot size was 40 μm–100 μm and the grain size was about 10 μm or smaller.)

The advantages of the integrated scan technique are that only a single spectrum, and usually a single peak, must be analyzed, and that the large probe automatically "averages" optically over the microstructure. Integrated scan techniques are thus more rapid and more easily implemented in determining average material parameters than two-dimensional mapping techniques. However, the integrated scan analysis method assumes a large, random distribution of grain orientations and a Gaussian stress distribution: the first is usually achieved by a large probe encompassing many grains, but the second is usually unproven. The two-dimensional mapping analysis method avoids the second drawback by assuming no specific form for the stress distribution but loses averaging simplicity by not assuming a completely random distribution of sampled grains. Comparison between the two techniques is made here by averaging in two different ways: First, by averaging *derived quantities* using two peaks pixel-by-pixel from the maps to form average stress parameters. Second, by averaging *raw spectra* to form an effective integrated scan and using a single peak to determine stress parameters. The work begins by reviewing the stress-optical analyses for fluorescence-based stress measurement in Al_2O_3 using two-dimensional maps and integrated scans; these analyses closely follow previous works [8,9,13]. Brief descriptions of the Cr-doped Al_2O_3 materials and hyperspectral imaging techniques used in the experiments are then provided; again, closely follow previous works [8]. Differences with previous works appear in the Results. The first Results section considers two-dimensional map results at increasing scale: initially as the spectrum from an individual pixel, then as maps of peak information from many spectra, then as stress information for a single material from many maps, and finally as average stress information for several materials. The second section of Results considers integrated scans, also in increasing scale: initially as a spectrum from a single scan, then as peak information from many scans, and then, finally, in the same form as the maps—permitting direct comparison—as mean

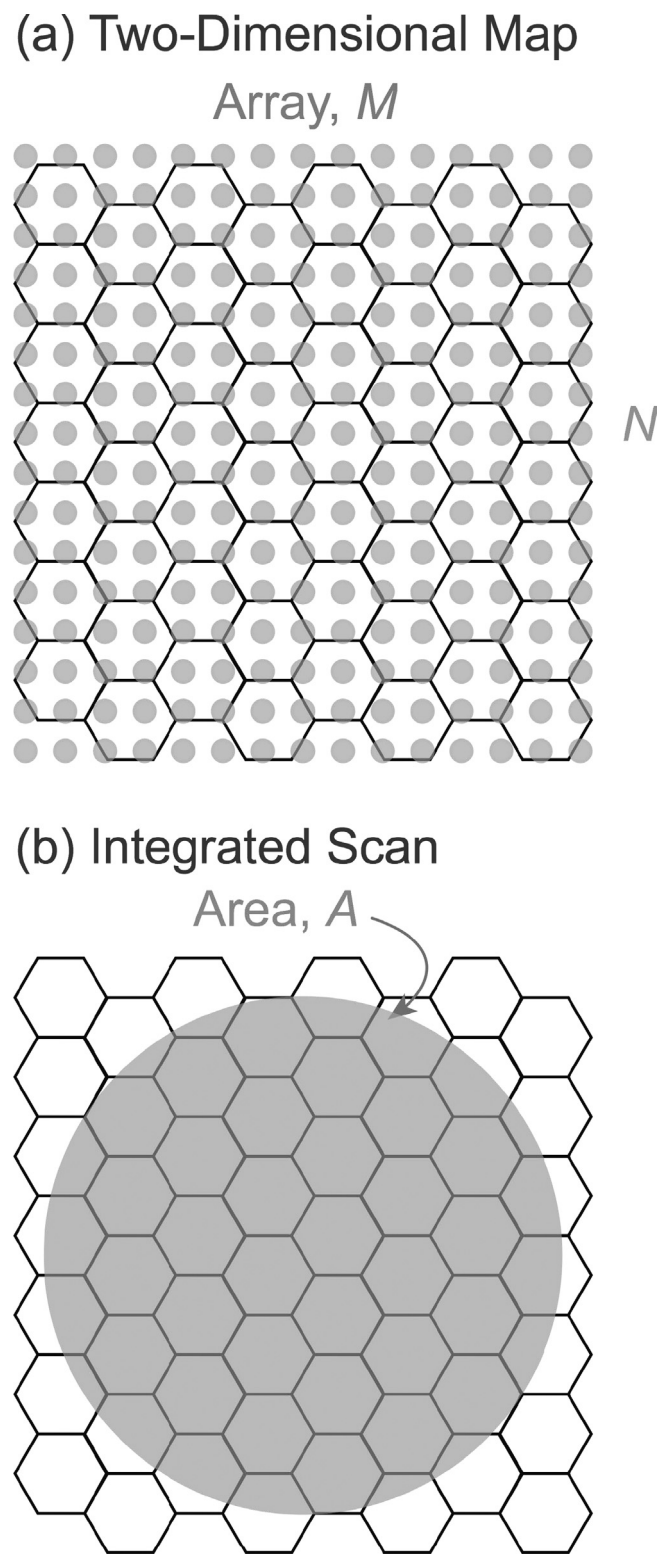

Fig. 1. Schematic diagrams of fluorescence-based techniques for determining stress in polycrystalline Al_2O_3. (a) Two-dimensional mapping using a hyperspectral array of multiple measurements. (b) Integrated scan using a large-area single measurement.

stress and dispersion information from scan results for several materials. Discussion centers on the nature of the comparison.

2. Analysis

2.1. Two-dimensional maps

The peak energies, $\nu^{(i)}$ (in wavenumbers, cm^{-1}), of the R_1 and R_2 fluorescent lines in Al_2O_3:Cr are given by

$$\nu^{(i)} = \nu_0^{(i)} + \Delta\nu_\sigma^{(i)} + \Delta\nu_T^{(i)} + \Delta\nu_C^{(i)}, \tag{1}$$

where the superscript $^{(i)}$ takes the values $^{(1)}$ or $^{(2)}$ indicating parameters associated with the R_1 or R_2 lines, respectively. The energies $\nu_0^{(i)}$ represent the peak positions of a reference material in the unstressed state at a temperature of 298.8 K with negligible Cr content. Here the reference material was taken as undoped sapphire, a corundum crystal [8]. The energies $\Delta\nu_\sigma^{(i)}$, $\Delta\nu_T^{(i)}$, and $\Delta\nu_C^{(i)}$ represent the shifts in peak position arising in a test material due to stress, temperature, and composition effects, respectively. The latter two shifts have simple scalar dependencies on temperature and composition and are given by

$$\Delta\nu_T^{(i)} = \beta_T^{(i)}(T - 298.8) \tag{2a}$$

$$\Delta\nu_C^{(i)} = \beta_C^{(i)}C, \tag{2b}$$

where T is the temperature in K, C is the composition in mass fraction of Cr in Al_2O_3:Cr, and $\beta_T^{(1)} = \beta_T^{(2)} = -0.140\ cm^{-1}/K$ and $\beta_C^{(1)} = \beta_C^{(2)} = 120\ cm^{-1}$/mass fraction are temperature and composition coefficients [5]. The shift due to stress has a general tensor dependency that is greatly simplified by the trigonal symmetry of the Al_2O_3 crystal structure, leading to

$$\Delta\nu_\sigma^{(i)} = \Pi_a^{(i)}(\sigma_{11} + \sigma_{22}) + \Pi_c^{(i)}\sigma_{33}, \tag{3}$$

where the tensor axes (1, 2, 3) correspond to the corundum crystallographic axes (a, m, c). The Π values are the piezospectroscopic coefficients and in corundum only those in Eq. (3) are non-zero, leading to four piezospectroscopic coefficients overall, $\Pi_a^{(1)} = 2.98\ cm^{-1}/GPa$, $\Pi_c^{(1)} = 1.64\ cm^{-1}/GPa$, $\Pi_a^{(2)} = 2.64\ cm^{-1}/GPa$, and $\prod_c^{(2)} = 2.32\ cm^{-1}$ [5], and a stress-optical shift equation, Eq. (3), for each peak with two degrees of freedom.

Re-arranging Eq. (3) gives

$$\Delta\nu_\sigma^{(i)} = \left(2\Pi_a^{(i)} + \Pi_c^{(i)}\right)\sigma_M + \left(\Pi_c^{(i)} - \Pi_a^{(i)} +\right)\sigma_S, \tag{4}$$

where

$$\sigma_M = (\sigma_{11} + \sigma_{22} + \sigma_{33})/3 \tag{5a}$$

is a local mean or spherical stress, and

$$\sigma_S = (2\sigma_{33} - \sigma_{11} - \sigma_{22})/3 \tag{5b}$$

is a local shear stress. Writing

$$\Pi_M^{(i)} = 2\Pi_a^{(i)} + \Pi_c^{(i)} \tag{6a}$$

$$\Pi_S^{(i)} = \Pi_c^{(i)} - \Pi_a^{(i)} \tag{6b}$$

enables Eq. (4) to be written in matrix form for each peak as

$$\begin{bmatrix} \Delta\nu_\sigma^{(1)} \\ \Delta\nu_\sigma^{(2)} \end{bmatrix} = \begin{bmatrix} \Pi_M^{(1)} & \Pi_S^{(1)} \\ \Pi_M^{(2)} & \Pi_S^{(2)} \end{bmatrix} \begin{bmatrix} \sigma_M \\ \sigma_S \end{bmatrix}. \tag{7}$$

Eq. (7) inverts to allow two components of the local stress field (σ_M, σ_S) to be determined from two local shift measurements ($\Delta\nu^{(1)}$, $\Delta\nu^{(2)}$) as

$$\begin{bmatrix} \sigma_M \\ \sigma_S \end{bmatrix} = \frac{1}{\Pi_M^{(1)}\Pi_S^{(2)} - \Pi_S^{(1)}\Pi_M^{(2)}} \begin{bmatrix} \Pi_S^{(2)} & -\Pi_S^{(1)} \\ -\Pi_M^{(2)} & \Pi_M^{(1)} \end{bmatrix} \begin{bmatrix} \Delta\nu_\sigma{}^{(1)} \\ \Delta\nu_\sigma{}^{(2)} \end{bmatrix} \tag{8}$$

Eq. (8) also pertains to the average stress values ($\overline{\sigma}_M, \overline{\sigma}_S$) that are related to the average shift values ($\overline{\Delta\nu_\sigma^{(1)}}, \overline{\Delta\nu_\sigma^{(2)}}$) by

$$\begin{bmatrix} \overline{\sigma}_M \\ \overline{\sigma}_S \end{bmatrix} = \frac{1}{\Pi_M^{(1)}\Pi_S^{(2)} - \Pi_S^{(1)}\Pi_M^{(2)}} \begin{bmatrix} \Pi_S^{(2)} & -\Pi_S^{(1)} \\ -\Pi_M^{(2)} & \Pi_M^{(1)} \end{bmatrix} \begin{bmatrix} \overline{\Delta\nu_\sigma^{(1)}} \\ \overline{\Delta\nu_\sigma^{(2)}} \end{bmatrix}, \tag{9}$$

where the overbar, $\overline{x}$, indicates the average of quantity x over a two-dimensional $M \times N$ map. Eq. (9) permits a direct experimental test of the equilibrium condition $\overline{\sigma}_M = 0$.

Alternatively, Eq. (3) many be re-written in terms of the average shifts and average crystallographic stresses ($\overline{\sigma}_a, \overline{\sigma}_c$) as

$$\overline{\Delta\nu_\sigma^{(i)}} = 2\Pi_a^{(i)}\overline{\sigma}_a + \Pi_c^{(i)}\overline{\sigma}_c \tag{10}$$

which may be expressed in matrix form and inverted similar to the above to give

$$\begin{bmatrix} \overline{\sigma}_a \\ \overline{\sigma}_c \end{bmatrix} = \frac{1}{2\Pi_a^{(1)}\Pi_c^{(2)} - 2\Pi_a^{(2)}\Pi_c^{(1)}} \begin{bmatrix} \Pi_c^{(2)} & -\Pi_c^{(1)} \\ -2\Pi_a^{(2)} & 2\Pi_a^{(1)} \end{bmatrix} \begin{bmatrix} \overline{\Delta\nu_\sigma^{(1)}} \\ \overline{\Delta\nu_\sigma^{(2)}} \end{bmatrix}. \tag{11}$$

Eq. (11) permits a direct experimental test of an alternative expression of the equilibrium condition, $\overline{\sigma}_c/\overline{\sigma}_a = -2$ [9], and direct comparison with the integrated scan methodology. Eq. (11) relates the mean shifts and mean crystallographic stresses and is globally exact, but may be relaxed to provide a local measurement if the local crystallographic stress field can be approximated as transversely isotropic consisting of two components, $\sigma_{11} = \sigma_{22} = \sigma_a$ and $\sigma_{33} = \sigma_c$, leading to

$$\begin{bmatrix} \sigma_a \\ \sigma_c \end{bmatrix} = \frac{1}{2\Pi_a^{(1)}\Pi_c^{(2)} - 2\Pi_a^{(2)}\Pi_c^{(1)}} \begin{bmatrix} \Pi_c^{(2)} & -\Pi_c^{(1)} \\ -2\Pi_a^{(2)} & 2\Pi_a^{(1)} \end{bmatrix} \begin{bmatrix} \Delta\nu_\sigma^{(1)} \\ \Delta\nu_\sigma^{(2)} \end{bmatrix}. \tag{12}$$

Eq. (12) allows two components of the local stress field (σ_a, σ_c) to be approximated from two local shift measurements ($\Delta\nu^{(1)}, \Delta\nu^{(2)}$).

In both cases of local stress mapping, Eqs. (8) and (12), statistical measures of the derived array of stress quantities, *e.g.*, means and standard deviations, can be determined from calculations involving the multiple individual pixels forming a map. Eqs. (9) and (11) show that the mean stress values, *e.g.*, $\overline{\sigma}_a$, are linearly related to the mean shifts and hence calculation and transformation between either is straightforward. Analysis of variance is required to transform between the standard deviations of the two distributions. In this work sd(x) indicates the standard deviation of quantity x calculated directly from a two-dimensional $M \times N$ map data, *e.g.*, sd (σ_a). Hence, a statistical description of the distribution of quantity x within a two-dimensional map is $\overline{x} \pm$ sd(x).

2.2. Integrated scans

An integrated scan may be formed by summing spectra from within an array to form an average spectrum, $I_A(\nu)$,

$$I_A(\nu) = \frac{1}{MN}\sum_{i,j=1}^{M,N} I_{ij}(\nu) \tag{13}$$

where $I_{ij}(\nu)$ is a spectrum from a single pixel within the $M \times N$ hyperspectral array. For $M \times N$ large, Eq. (13) approaches an integral over the discretely mapped area A [8]. The peak energies, $\nu_A^{(i)}$ of the R_1 and R_2 fluorescent lines within the average spectrum of the integrated scan are given by

$$\nu_A^{(i)} = \nu_0^{(i)} + \Delta\nu_{A\sigma}^{(i)} + \overline{\Delta\nu}_T^{(i)} + \Delta\nu_C^{(i)} \tag{14}$$

where, as before, the superscript $^{(i)}$ takes the values $^{(1)}$ or $^{(2)}$ and $\nu_0^{(i)}$ represents the peak positions of the reference material. $\overline{\Delta\nu}_T^{(i)}$ and $\Delta\nu_C^{(i)}$ represent the changes in energies of the peaks due to temperature effects (averaged over the array) and composition effects (assumed homogeneous), respectively. The energies $\Delta\nu_{A\sigma}^{(i)}$ represent the changes in the single integrated peak position due to stress effects. As Eq. (13) is an intensity summation, the energy change $\Delta\nu_{A\sigma}^{(i)}$, Eq. (14), reflects the cumulative effects of intensity-weighted array elements within the integrated scan area. This is not true of the two-dimensional map approach, which calculates an unweighted mean energy change $\overline{\Delta\nu}_\sigma^{(i)}$. In addition, a true integrated scan measurement would likely sample a greater depth than the two-dimensional array measurements, capturing the spectral response of subsurface material that is omitted by the reconstruction of Eq. (13).

Obviously, $\Delta\nu_{A\sigma}^{(1)}$ and $\Delta\nu_{A\sigma}^{(2)}$ can be used in Eq. (8) or (11) to obtain estimates of the mean stresses $(\overline{\sigma}_M, \overline{\sigma}_S)$ or $(\overline{\sigma}_a, \overline{\sigma}_c)$. This is a two-peak method of integrated scan stress analysis although it is generally not used. No statistical measure of stress distribution as described above is available from a single average spectrum. Most integrated scan analysis methods, however, use a single peak and restrict attention to the crystallographic stresses by re-writing Eq. (3) as

$$\Delta\nu_{A\sigma}^{(i)} = 2\Pi_a^{(i)}\overline{\sigma}_a + \Pi_c^{(i)}\overline{\sigma}_c \tag{15}$$

and *imposing* the equilibrium condition $\overline{\sigma}_c/\overline{\sigma}_a = -2$ to arrive at [10].

$$\overline{\sigma}_c = -2\overline{\sigma}_a = \Delta\nu_{A\sigma}^{(i)} \Big/ \left(\Pi_c^{(i)} - \Pi_a^{(i)}\right). \tag{16}$$

Eq. (16) provides two estimates (R_1 and R_2) of the set of mean crystallographic stresses $(\overline{\sigma}_a, \overline{\sigma}_c)$. It is noted that within each set, the mean stresses are not independent as they are linked by the assumed equilibrium condition.

The distributions of stresses about the mean values estimated from an integrated scan are *assumed* to be Gaussian, with common standard deviation σ_W [4,8,10]. The standard deviation is estimated from the increased widths of the integrated scan peaks from the polycrystalline material (R_1 and R_2) relative to those from the reference material. The reference material peak widths are dominated by thermal broadening, with no difference between map and integrated scan values, and have half widths at half heights given by $HWHH_0^{(i)}$. Single-spot peak widths taken from a polycrystalline material array are similar to the reference material values as both fluorescence peaks arise from within single crystals. However, integrated scan peak widths taken from a polycrystalline material reflect the convolution of the thermally-broadened single-spot fluorescence spectra with the range of peak positions from the many single-crystal grains sampled. Hence, polycrystalline material integrated scan peak widths are broadened from the reference values by microstructural stress effects to give $HWHH_A^{(i)}$. The difference between these two values is quantified by $\Gamma^{(i)}$, given by

$$\Gamma^{(i)} = \left[\left(HWHH_A^{(i)}\right)^2 - \left(HWHH_0^{(i)}\right)^2\right]^{1/2} \tag{17}$$

and is related to the change in the second moment of the integrated scan peak intensities [8,10]. The standard deviations of the stress distributions are then determined from this difference by

$$\sigma_W^{(i)} = \Gamma^{(i)}\left[4\left(\Pi_a^{(i)}\right)^2 - \left(\Pi_c^{(i)}\right)^2\right]^{-1/2} \tag{18}$$

In the case of integrated scan stress estimation, the statistical descriptions of the assumed Gaussian stress distributions within the scan area are given by mean ± standard deviation estimations of $\overline{\sigma}_a^{(i)} \pm \sigma_W^{(i)}$ and $\overline{\sigma}_c^{(i)} \pm \sigma_W^{(i)}$, noting that the means are not independent, Eq. (16), that the standard deviations are identical, Eq. (18), and that there are two estimations (R_1 and R_2) from each scan. These statistical descriptions can be used in direct comparison with the descriptions determined from the two-dimensional map analysis above.

3. Experimental methods

3.1. Materials

The stress states in a series of three polycrystalline Al_2O_3 materials were compared by fluorescence-based two-dimensional mapping and integrated scan techniques. The series was used in a previous extensive study of strength and toughness of polycrystalline Al_2O_3 [14] and in recent studies of fluorescence-based residual stress mapping [4,7,8]. The materials were deliberately doped with Cr by infusing porous pre-cursors with a chromate solution prior to sintering at 6 h, 12 h, and 18 h at 1600 °C in H_2. The sintered polycrystals were translucent pink in color, had greater than 99.5% relative density, and average Cr content of 0.025% expressed as the mass fraction of Cr in Al_2O_3:Cr. The mode grain sizes for the three sintering times were approximately 10 μm, 15 μm, and 20 μm, respectively, although the grain size distributions were broad and grains as large as 60 μm were observed. Sections of each material were polished for fluorescence measurements. The reference material was a single-crystal *c*-axis sapphire plate, also used earlier [4,8], stated to have >99.99% Al_2O_3 purity.

3.2. Hyperspectral fluorescence microscopy and analysis

The experimental apparatus used to acquire the 18 two-dimensional fluorescence maps of the various sintered alumina specimens discussed in this paper has been described in extensive detail previously [8]. The spectrum obtained at each spatial location consisted of fluorescence intensities recorded at 1340 points across the energy range shown in Fig. 2, requiring 5.4 kB (4 bytes per point). The acquisition time for each spectrum was 0.5 s which was sufficient to achieve signal-to-noise ratios of approximately 200:1. The two-dimensional maps consisted of 128 × 128 spectra acquired on an evenly spaced grid over an 80 μm × 80 μm area of the specimen, yielding a pixel spacing of 625 nm, roughly twice the diffraction limited lateral radius of the excitation laser beam spot, about 325 nm [8]. Combined with the axial information depth of

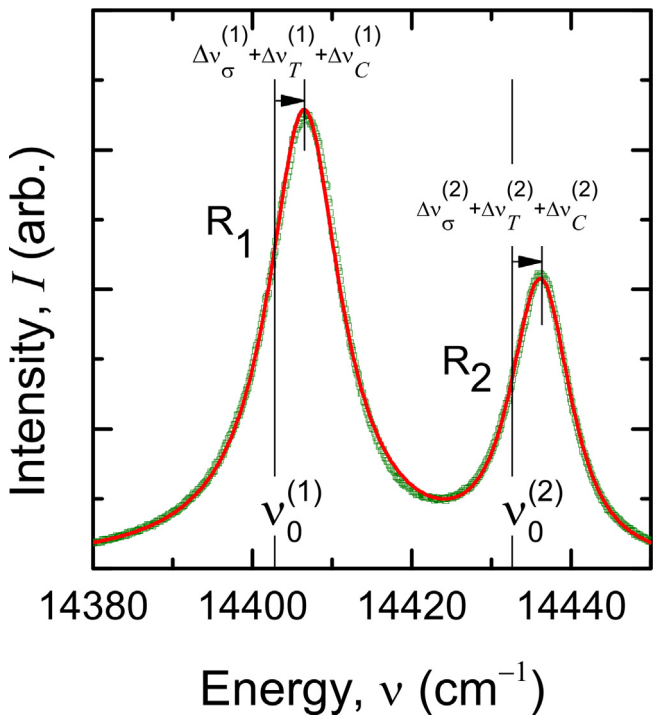

Fig. 2. Fluorescence spectrum obtained from a single pixel within a hyperspectral array on polycrystalline alumina. Measured intensity shown as symbols, fit shown as solid line. The R_1 and R_2 peaks are marked as are the peak positions of a reference crystal. The shifts due to stress, temperature, and composition effects are indicated.

the excitation, about 3 μm [8], the sampling volume/spectrum was thus about 1 μm^3 (much smaller than the map and grain volumes). The total time required for each two-dimensional map, including scanning time, was just under 10 h and each map required approximately 88.5 MB. Eighteen total maps were acquired (5 maps for the 6 h specimens, 8 maps for the 12 h, and 5 maps for the 18 h) summing to a total of about 1.6 GB of raw spectral data acquired over about 180 h.

All of the spectra, including those of the single crystal sapphire reference specimen and the integrated scan spectra defined in Eq. (13), were fit to a dual-peak Pearson VII model with fixed best-fit shape parameters, yielding peak amplitude, width, and center wavenumber parameters for R_1 and R_2. All peak center wavenumber values were corrected for temperature and composition as described in Eq. (2). The peak center wavenumber values were then used to determine $\Delta\nu_\sigma^{(i)}$ as described in Eq. (1) or $\Delta_{A\sigma}^{(i)}$ as described in Eq. (14). The peak data for each map required about 1.2 GB summing to a total of about 22 GB of analyzed spectral data.

4. Results

4.1. Two-dimensional maps

Fig. 2 is a plot of a typical fluorescence spectrum $I(\nu)$ obtained from a single central point (63, 63) in a two-dimensional hyperspectral array (128 × 128) of the 18 h polycrystalline Al_2O_3 material. The symbols show the measured intensity I as a function of photon energy ν and the solid line shows the best fit to the spectral model function. The two fluorescence peaks, R_1 and R_2, are indicated. The vertical lines indicate the peak intensity positions of the sapphire reference material, $\nu_0^{(1)}$ and $\nu_0^{(2)}$. The changes from the reference positions for the fluorescence peaks at this point in the polycrystalline material array due to stress, temperature, and composition effects, Eq. (1), are indicated. Spectra and fits from other points within this array and from within arrays on this and other materials were visually similar, with variations in the changes in the positions of the fluorescence peaks.

Characteristics of each peak at points in an array can be used to generate a pixel in a two-dimensional map. Fig. 3(a) is a (128 × 128) two-dimensional map of the R_1 peak intensity from the hyperspectral array of the 18 h polycrystalline Al_2O_3 material from which

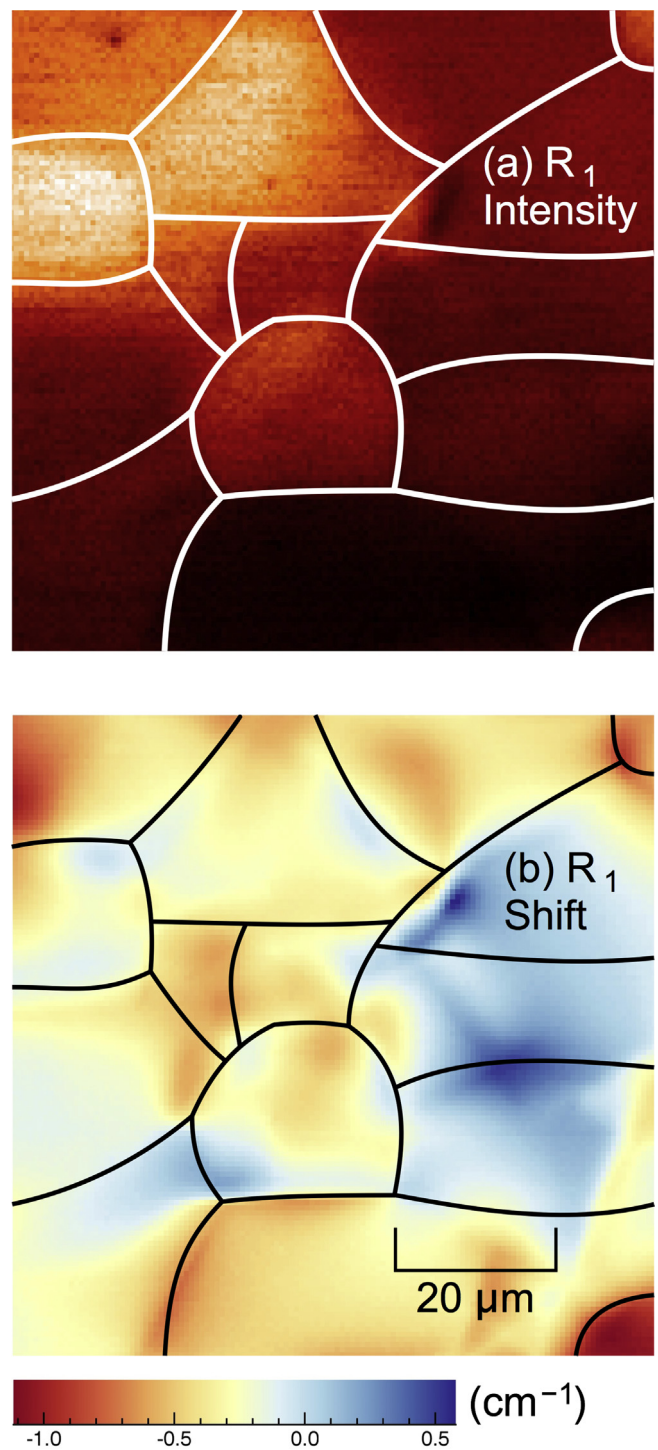

Fig. 3. (a) Map of R_1 fluorescence intensity for the 18 h alumina material with grains overlaid. (b) Map of R_1 peak shift over the same area.

Fig. 2 was taken. The separate corundum grains of the polycrystalline structure fluoresce with different intensity due to the sensitivity of the fluorescence emission to the relative orientation of the corundum crystal structure and the excitation polarization [15,16]. Advantage may be taken of this sensitivity to segment the microstructure into separate grains, either numerically [4] or visually [8]. As a guide to the eye, "grain boundaries" visually determined from changes in fluorescence intensity are indicated in Fig. 3(a) by solid lines. Obviously, such segmentation is not as sensitive as the direct crystallographic assessment of orientation determined by EBSD [7], but it does provide a microstructural scale to assess stress and other variations. Fig. 3(b) is a map of the stress-related shift of the R_1 peak, $\Delta\nu_\sigma^{(1)}$, *i.e.*, "corrected" pixel by pixel for temperature and composition effects, Eq. (1), of the same area as Fig. 3(a). The grain boundaries inferred from the intensity map, Fig. 3(a), are superposed. Both positive and negative shifts were observed and, as in previous studies [4,7,8], the correlation between shift and grain structure was weak. Other intensity and shift maps, based on both R_1 and R_2, from this and other materials were similar.

The full range of stress-related shifts in pictorial two-dimensional maps such as Fig. 3(b) can be condensed into one-dimensional histograms of shifts, providing quantitative overviews of maps. Fig. 4(a) shows the R_1 shift histogram appropriate to Fig. 3(b) as the bold solid line. The histogram is somewhat scattered and although overall unimodal is clearly composed of several overlapping sub-peaks giving rise to "shoulders" on the unimodal outline. The sub-peaks probably represent the separate grain areas visible in Fig. 3(b). Other maps and arrays produced similar results and Fig. 4(a) shows the shift histograms from the other maps generated on the 18 h material as grayed lines. The broad similarity of the full set of histograms is clear and the grayed lines form an envelope that describes the full R_1 response. A similar plot and envelope is shown in Fig. 4(b) for the R_2 shift histograms; the bold and grayed lines represent the same mapped areas as in Fig. 4(a). Taken together, the envelopes of Fig. 4 describe the overall 18 h material fluorescence response.

Fig. 5 combines the $\Delta\nu_\sigma^{(1)}$ map information of Fig. 3(b) with similar $\Delta\nu_\sigma^{(2)}$ information (not shown) using Eq. (8) to show σ_M and σ_S maps from the same area of the 18 h polycrystalline material as in Figs. 3 and 4. The grain boundaries inferred from the intensity map, Fig. 3(a), are superposed. Note that the stress scales and color maps in Fig. 5(a) and (b) are different. Both tensile and compressive stress regions were observed in the spherical stress map, Fig. 5(a). The variation of stress in the shear stress map, Fig. 5(b) appears greater than in the spherical stress map, and, once again, the correlation between stress and grain structure was often weak [4,7,8,17,18]. Fig. 6 condenses the pictorial map data of Fig. 5 into one-dimensional histograms shown as the bold solid lines. The histograms are somewhat scattered and again are clearly composed of several overlapping sub-peaks representing the separate grain areas visible in Fig. 5. Other stress maps produced similar results and Fig. 6 shows the stress histograms from the other maps generated on the 18 h material as grayed lines. The full sets of histograms form envelopes that describe the stress state of the 18 h material and, as noted previously [4,8] although unimodal and symmetric are only approximately Gaussian.

The complete set of stress maps derived from the hyperspectral arrays, including (σ_M, σ_S) and (σ_a, σ_c), for all three materials, 6 h, 12 h, and 18 h, were similar to those of Fig. 5, although σ_a was predominantly compressive and σ_c was predominantly tensile. Condensation of the two-dimensional maps into one-dimensional histograms for each material led to envelopes similar to Fig. 6. The map and histogram for each array can be further condensed

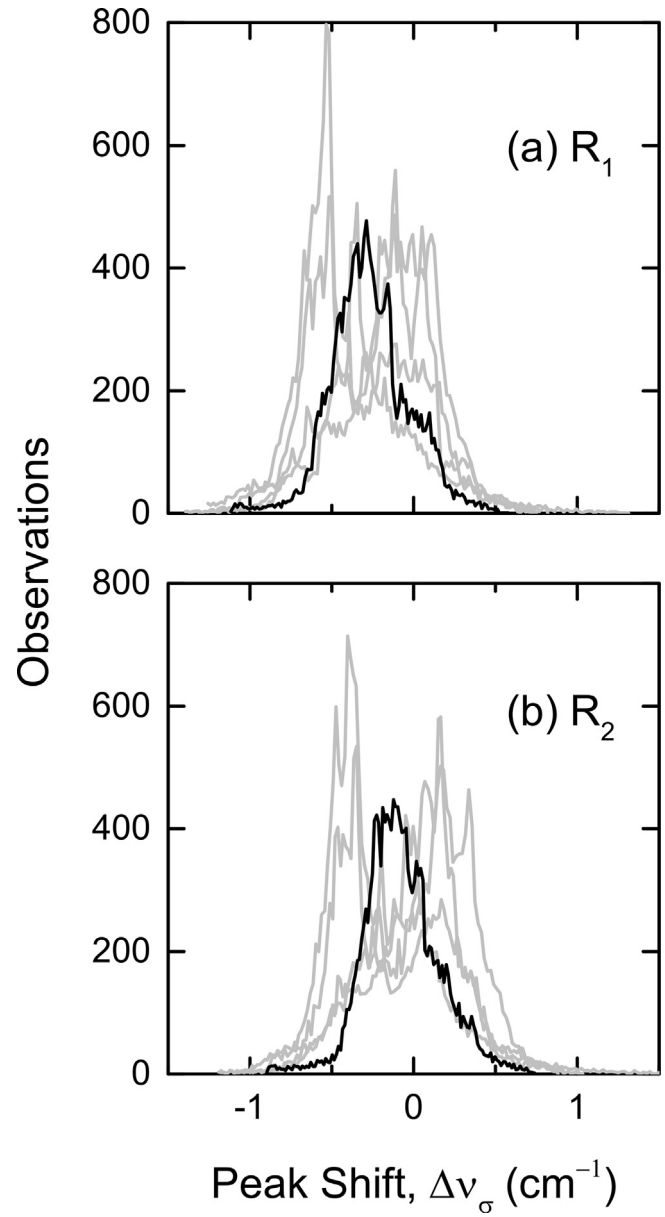

Fig. 4. (a) Histograms of the R_1 fluorescence shifts for the 18 h alumina material; area from Fig. 3 marked in black, others in gray. (b) Histograms of the R_2 fluorescence shifts for the 18 h alumina material as in (a).

and characterized by a mean and standard deviation of the stress distribution. The vertical dashed lines in Fig. 6 show an example of means and standard deviation limits, appropriate to the solid-line histograms. In this case the means correspond to $\overline{\sigma}_M$ and $\overline{\sigma}_S$. Fig. 7 shows the complete set of means and standard deviations for all stresses on all materials; $\overline{\sigma}_M$ and $\overline{\sigma}_S$, Fig. 7(a) and $\overline{\sigma}_a$ and $\overline{\sigma}_c$, Fig. 7(b). Each symbol represents a value determined from a separate ($128 \times 128 = 16\,384$) two-dimensional stress map; the symbols within each material group are ordered for ease of visualization by increasing $\overline{\Delta\nu_\sigma^{(1)}}$ (not shown).

The horizontal solid line in Fig. 7(a) represents the equilibrium condition $\overline{\sigma}_M = 0$. The experimental observations for all materials clearly cluster about this line and in only two cases do the standard deviation limits of an individual map fail to encompass this value. Recalling that there are no adjustable factors in the analysis, the $\overline{\sigma}_M$

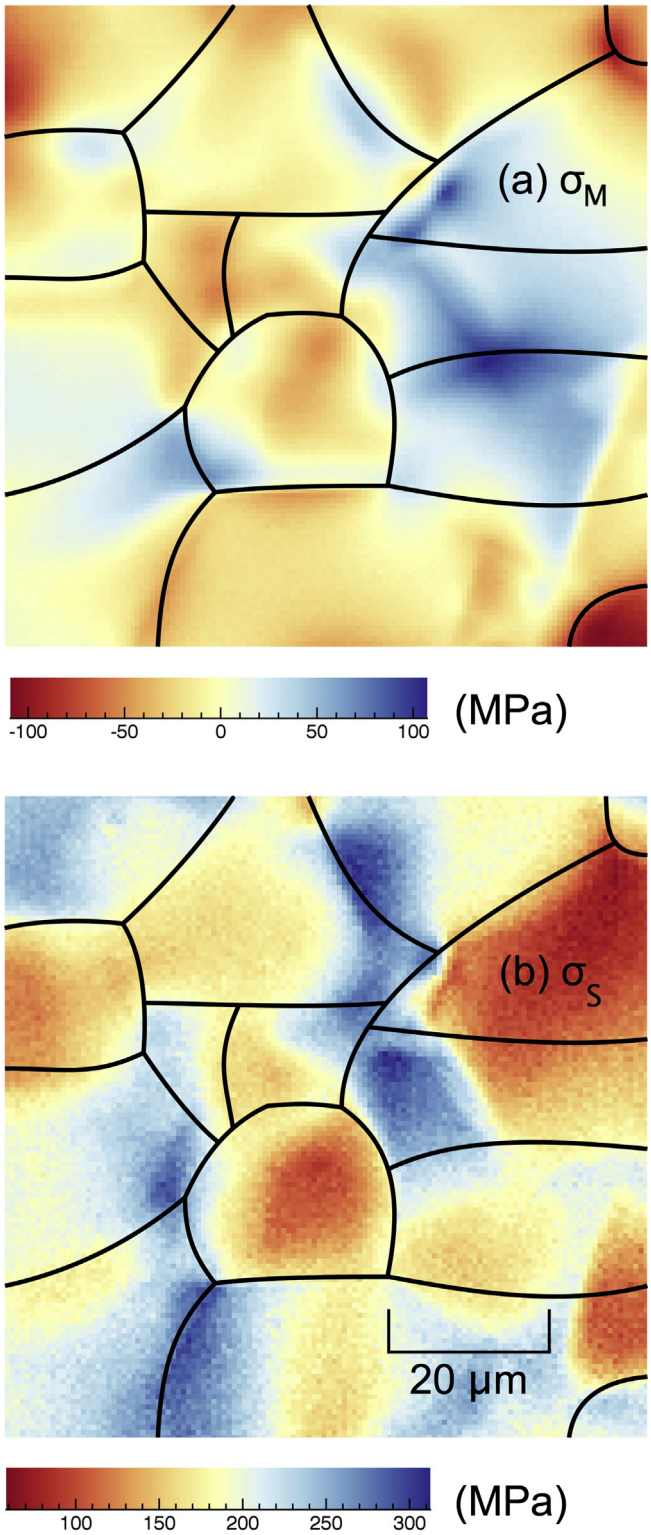

Fig. 5. (a) Map of σ_M spherical stress for the 18 h alumina material from the same area as Fig. 3. (b) Map of σ_S shear stress for the 18 h alumina material from the same area as (a).

observations of Fig. 7(a) provide great support for the fluorescence-based stress measurement technique as the deconvoluted spherical stress values, as noted previously [8], are consistent with mechanical equilibrium. The increasing trend within each material group for $\overline{\sigma}_M$ suggests a correlation with $\overline{\Delta\nu}_\sigma^{(1)}$. This trend was not in

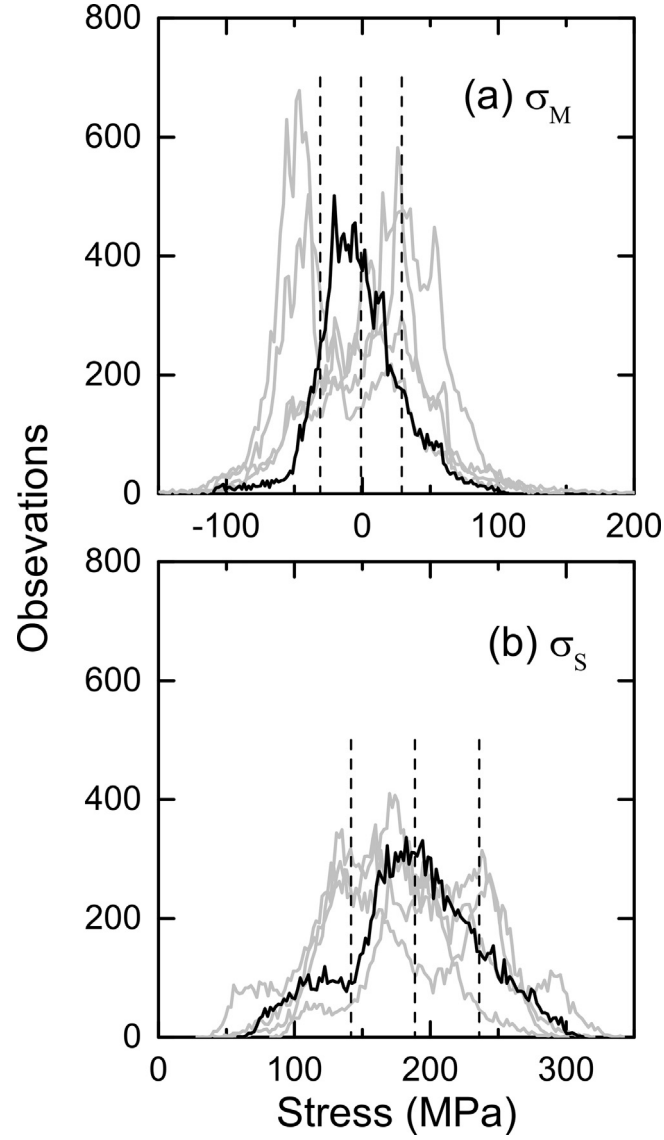

Fig. 6. (a) Histograms of the σ_M stress for the 18 h alumina material; area from Fig. 5 marked in black, others in gray. (b) Histograms of the σ_S stress for the 18 h alumina material as in (a). Means and standard deviations for Fig. 5 data marked as dashed vertical lines.

evidence in the $\overline{\sigma}_S$ data, which clustered for all materials about ≈ 175 MPa, suggesting some commonality in the stress state, consistent with the similar material processing and microstructures. The $\overline{\sigma}_a$ and $\overline{\sigma}_c$ data of Fig. 7(b) also exhibit increasing trends within each material group consistent with correlations with $\overline{\Delta\nu}_\sigma^{(1)}$. As a guide to the eye, the upper shaded band in Fig. 7(b) indicates the range (190 ± 40) MPa; this range encompasses the standard deviation limits of all the $\overline{\sigma}_c$ observations, consistent with microstructural and stress state similarity across material groups. Consistent with the alternative statement of equilibrium, that $\overline{\sigma}_a = -\overline{\sigma}_c/2$, the lower shaded band in Fig. 7(b) indicates the range (-95 ± 20) MPa; this range encompasses the standard deviation limits of all the $\overline{\sigma}_a$ observations, further supporting the measurement technique as the ratio of the deconvoluted crystallographic stress values are consistent with mechanical equilibrium, also noted previously [8]. The highly-condensed, two-dimensional map data of Fig. 7(b) are the basis for comparison with the integrated scan data.

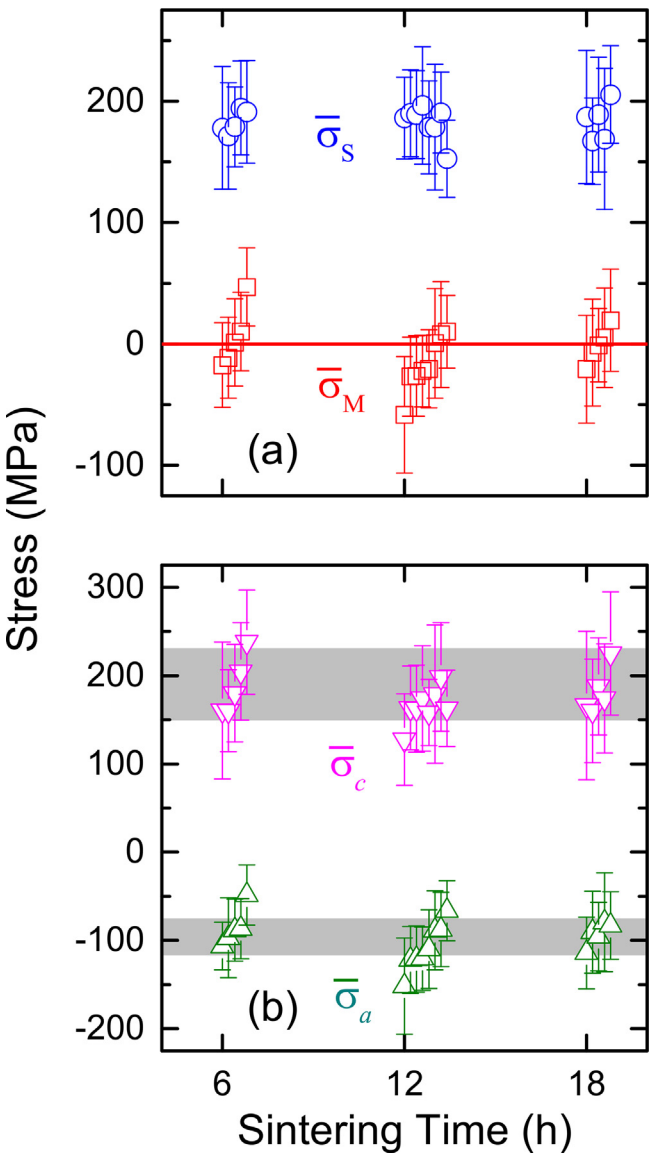

Fig. 7. (a) Plot of average spherical stress, $\bar{\sigma}_M$, and average shear stress, $\bar{\sigma}_S$, determined from two-dimensional fluorescence maps of alumina sintered for 6 h, 12 h, and 18 h. Separate symbols represent separate mapped areas; data offset for clarity. The solid line indicates zero stress. (b) Plot of average crystallographic stresses, $\bar{\sigma}_c$ and $\bar{\sigma}_a$, determined from two-dimensional fluorescence maps of alumina sintered for 6 h, 12 h, and 18 h. Separate symbols represent separate mapped areas; data offset for clarity. The shaded bands indicate the approximate stress ranges, consistent with the equilibrium condition $\bar{\sigma}_c = -2\bar{\sigma}_a$.

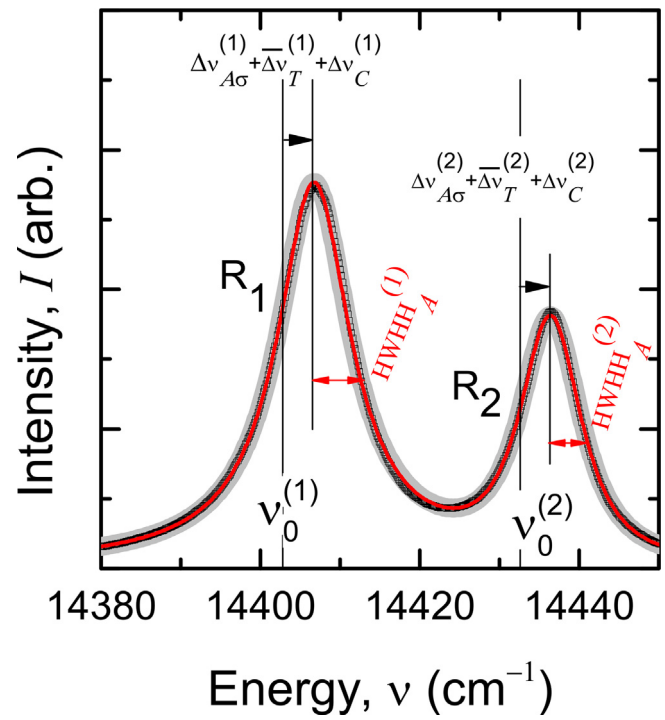

Fig. 8. Integrated scan fluorescence spectrum obtained by averaging multiple spectra within a hyperspectral array on polycrystalline alumina. Measured intensity shown as symbols, fit shown as solid line, envelope of contributing spectra shown as grayed band. The R_1 and R_2 peaks and the peak positions of a reference crystal are marked. The shifts due to stress, temperature, and composition effects are indicated along with the half width at half height (HWHH) of the peaks.

4.2. Integrated scans

Fig. 8 shows the single fluorescence spectrum, $I_A(\nu)$, obtained from the 18 h material hyperspectral data underlying Figs. 3–7, of which the experimental data of Fig. 2 form part. The shaded gray band in Fig. 8 shows the approximate range of ($128 \times 128 = 16\,384$) spectral positions (about $\pm 1\,\text{cm}^{-1}$, see Fig. 3) comprising the average of Eq. (13). The symbols in Fig. 8 indicate the average integrated scan spectrum; the solid line shows the fit. The two fluorescence peaks, R_1 and R_2, are indicated, along with the peak positions of the sapphire reference material, $\nu_0^{(1)}$ and $\nu_0^{(2)}$, and the changes from the reference positions for the integrated scan peaks. Visually, the integrated scan spectrum of Fig. 8 looks much the same as the single point spectrum of Fig. 2, a consequence of averaging very similar spectra. Close inspection of Figs. 2 and 8, however, shows that the integrated scan spectrum is somewhat broader than the single point spectrum due to the convolution effects noted above. Also indicated in Fig. 8 are the half width at half height values for the peaks ($HWHH_A^{(i)}$) to be used in stress distribution analysis. Integrated scan spectra and fits from other arrays on this and other materials were visually similar, with variations in the changes in positions and widths of the fluorescence peaks.

Fig. 9 compares the raw-data peak characteristics from the two-dimensional map analysis and the integrated scan analysis. In Fig. 9(a), the peak-intensity energy changes from the integrated scans, $\Delta\nu_{\sigma A}^{(i)}$, are plotted *vs* the mean peak-intensity energy changes from the maps, $\overline{\Delta\nu_{\sigma}^{(i)}}$. For each of R_1 and R_2, the first value quantifies the energy change of the single peak from the average of 16 384 *spectra* whereas the second quantifies the average of the energy changes from 16 384 *peaks*. The results from the 18 arrays are shown as the symbols in Fig. 9(a) and are consistent with equality of these two quantities as indicated by the solid line. The implications of this equality are two-fold: First, it appears to make no difference in the determination of the mean energy shifts when averaging is performed on the hyperspectral array data, before peak fitting (integrated scan method) or after peak fitting (two-dimensional map method). Second, a *two-peak* analysis, Eq. (9) or (11), for the *mean* stress within a single array will return near-identical results from the integrated scan method and the two-dimensional map method.

The map method of course can also provide explicit peak-energy distribution information for an array (*e.g.*, Fig. 4), whereas the integrated scan method cannot. The integrated scan method does, however, provide information regarding an assumed Gaussian underlying peak-energy distribution from the change in width of

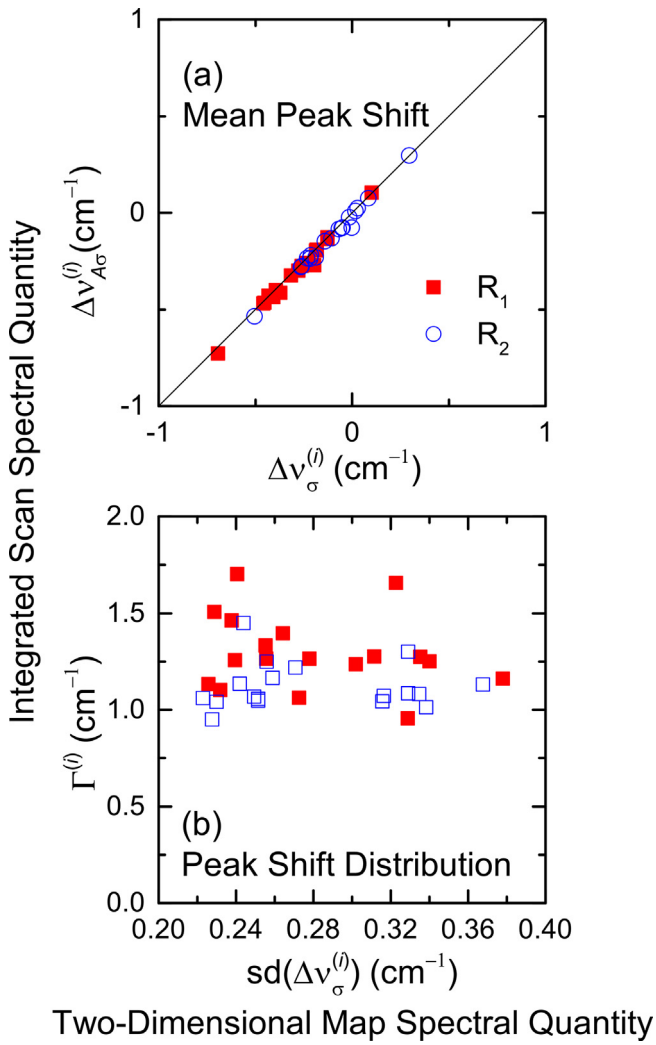

Fig. 9. Plot of spectral quantities obtained from integrated scans *vs* analogous quantities obtained from two-dimensional maps of fluorescence measurements on alumina. (a) Mean peak shift. Measurements shown as symbols. Ideal agreement shown as the solid line. (b) Peak shift distribution width. Gaussian standard deviation inferred from integrated scan, standard deviation measured from two-dimensional map.

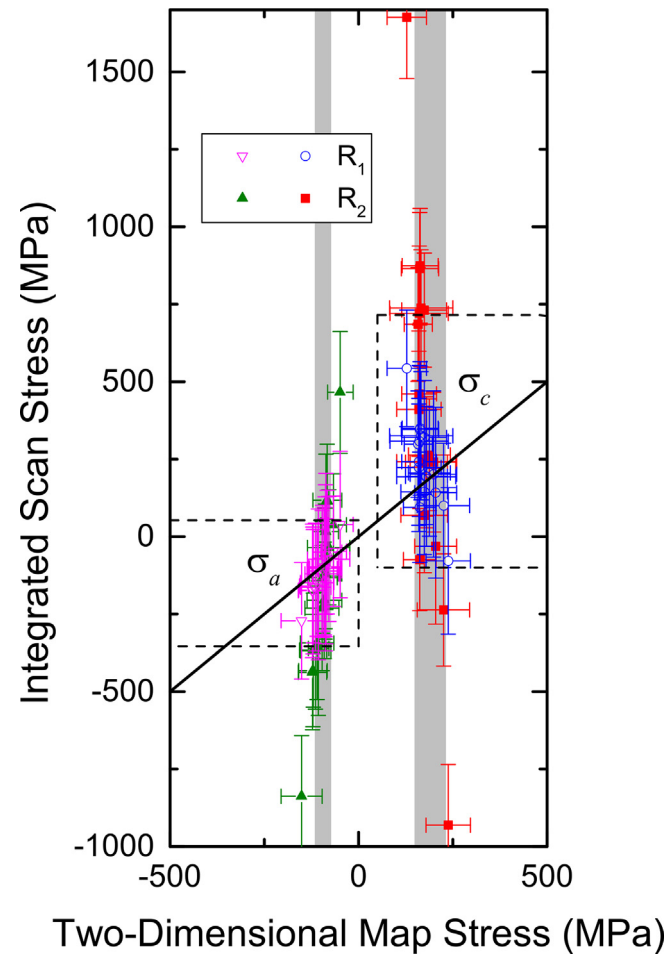

Fig. 10. Plot of crystallographic stress quantities obtained from integrated scans *vs* analogous quantities obtained from two-dimensional maps of fluorescence measurements on alumina. Symbols represent estimations from 18 separate areas on three materials. The solid line indicates ideal agreement. The vertical shaded bars indicate the ranges of values determined from the two-dimensional map measurements (Fig. 6). The vertical limits of the dashed boxes indicate standard deviation limits of the integrated scan data. Overall, integrated scan estimations agree with two-dimensional maps estimations, although the uncertainty is large.

the single peak relative to a reference material peak, Eq. (17). Fig. 9(b) is a plot of the parameters $\Gamma^{(i)}$ obtained from the integrated scans and previous reference material measurements [8], characterizing the changes in peak widths, *vs* the parameters sd $(\nu^{(i)})$ obtained from the two-dimensional maps, giving the standard deviations of the peak distributions. The first point to note about Fig. 9(b) is that the $\Gamma^{(i)}$ values lie between 1.0 cm^{-1} and 1.5 cm^{-1}, compared with $HWHH_0^{(i)} \approx 5\ cm^{-1}$ [8], consistent with the observation that the integrated scan peaks (Fig. 8) appear very similar to a single array element map peak (Fig. 2). The second point to note is that the $\Gamma^{(i)}$ values exhibit no trend with sd $(\nu^{(i)})$, which ranges over a factor of two, from $\approx 0.2\ cm^{-1}$ to $\approx 0.4\ cm^{-1}$, and that there is no significant difference between $\Gamma^{(1)}$ and $\Gamma^{(2)}$. The expectation therefore from Eq. (18) is that the standard deviations of the assumed stress distributions will be relatively invariant.

The focus here is on comparison of the stress distributions inferred from the traditional *single-peak* integrated scan analysis, with those inferred from two-peak two-dimensional map analyses. Fig. 10 is a plot of $\overline{\sigma}_a^{(i)} \pm \sigma_w^{(i)}$ and $\overline{\sigma}_c^{(i)} \pm \sigma_w^{(i)}$, obtained using the data from Fig. 9 and Eqs. (16) and (18), *vs* $\overline{\sigma}_a \pm$ sd (σ_a) and $\overline{\sigma}_c \pm$ sd (σ_c), respectively, using the data from Fig. 7(b). Note that although the plot is asymmetric, the scales on the plot axes are identical. The symbols represent measurements from individual maps or scans; the correlations of the mean values arise from the use of common Π values. The solid line shows ideal agreement. The shaded bands in the plot are the same "guide to the eye" bands as drawn in Fig. 7, here rendered vertically and indicating the approximate ranges of $\overline{\sigma}_a$ and $\overline{\sigma}_c$ determined from the two-dimensional map analyses. The increased ranges of the stresses obtained from the integrated scan analyses are indicated by the nearly 3:1 aspect ratio of the plot: the mean stress estimates are distributed over much greater ranges of approximately 2000 MPa compared with approximately 60 MPa exhibited by the two-dimensional mapping analysis and the distributions about these means are characterized by much greater standard deviations of approximately 200 MPa, compared with approximately 50 MPa exhibited by the two-dimensional mapping analysis. On average, the integrated scan estimates agree with the two-dimensional map estimates, as shown by the upper and lower limits of the dashed boxes in Fig. 10, which indicate standard deviation limits of the (unweighted) mean stress estimates from the integrated scan analysis. These limits, (-154 ± 203) MPa and (308 ± 407) MPa for $\overline{\sigma}_a$ and $\overline{\sigma}_c$, respectively, overlie the intersections

of the ideal-agreement line with the shaded bands, (-95 ± 20) MPa and (190 ± 40) MPa, respectively.

5. Discussion and conclusions

A conclusion that *can* be drawn from the above extensive investigation of polycrystalline Al_2O_3 using fluorescence techniques is that stress estimates using the two-peak-based two-dimensional map method agree with the traditional one-peak-based integrated scan method. Such agreement was demonstrated previously on one mapped area on one material [8] but the 18 total mapped areas on three materials studied here provide greater insight. In particular, the agreement is seen to be somewhat statistical: the estimated magnitudes of the mean crystallographic stresses from the integrated scan method were approximately a factor of 1.5 times greater than those estimated from the two-dimensional map method. This factor was about three times the relative ranges (and standard deviations) of the measured distributions of stresses in the two-dimensional maps and represents marginal agreement of the mean values. However, the standard deviations of the mean values estimated from the multiple integrated scans were about a factor of 10 greater than these ranges, enabling statistical agreement of the mean values. A problem of physical consistency arises with the use of these standard deviations however, in that the inferred distributions of stresses around the means include a significant proportion of stresses of opposite sign to the mean value (see Fig. 10)—a characteristic of the distributions *not* observed in direct measurements of map data [4,6–8]. This problem also extends to single scans in which the inferred widths of assumed Gaussian distributions include significant proportions of stresses of opposite signs [8,9].

The resolution to the above analysis problems that retains the convenience of single integrated scan measurements is to use *two-peak*, rather than single peak, analyses on integrated scans. Fig. 9(a) suggests that two-peak analysis of integrated scan spectra (Fig. 8) would return near-identical estimates of *average* stress pairs ($\overline{\sigma}_M$, $\overline{\sigma}_S$) and ($\overline{\sigma}_a$,$\overline{\sigma}_c$) to those estimated from two-dimensional maps. The uncertainty of these average estimates could be determined from the standard error of multiple integrated scan determinations. The *distributions* of stresses about these averages could be estimated by revising Eq. (18) empirically to read

$$\sigma_w^{(i)} \approx \left(\Gamma^{(i)}/4\right)\left[4\left(\Pi_a^{(i)}\right)^2 - \left(\Pi_c^{(i)}\right)^2\right]^{-1/2}, \tag{18a}$$

to give the standard deviations of assumed Gaussian stress distributions, Fig. 9(b). A recent review suggests that the uncertainties in the standard error of the mean values and the standard deviation of the distributions derived from Type-A statistical components of measurements will be large relative to Type-B systematic uncertainties in the coefficients [5]. Of course, measurements on a reference material and corrections for temperature and composition are still required, all contributing to Type-B uncertainty.

Although the present work has largely focused on spectroscopic comparisons, spatial comparisons are also important. Three length scales are considered. At the smallest scale, surface reconstruction usually extends a few crystalline layers into the material. Both hyperspectral map and integrated scan techniques have information depths many orders of magnitude larger than these layers and, in this sense, the measurements here and elsewhere overwhelmingly sample bulk material and are unperturbed by surface effects. At microstructural scales, residual stress fluctuations appear to extend a few grains (Fig. 5), but averaging over many grains, from area to area in a microstructure (here, separated by about 100 μm), appears to lead to variations in mean residual stress across a specimen comparable to the width of the fluctuations (here, about 100 MPa, Fig. 7). Only hyperspectral map techniques sense this variation. At the largest scale, mechanical equilibrium requires the surface to be traction free. The transition from bulk to surface is dependent on specimen homogeneity and for homogeneous materials (as here) the depth transition is expected to occur within the above reconstruction layer and both hyperspectral map and integrated scan techniques are unperturbed. For inhomogeneous systems (*e.g.*, adjacent to interfaces), the transition usually occurs over the scale of the inhomogeneity and hyperspectral map techniques would be preferentially perturbed. Microstructural spatial variations are currently under study by statistical techniques. Depth effects could be studied by varying the numerical aperture of illumination and collection.

Finally, a major goal—to enable fluorescence measurements of the microstructural dependence of residual stress development in polycrystalline Al_2O_3—appears to have been achieved. Previous integrated scan measurements had the advantage of speed, ease of analysis, and automatic averaging over large volumes of the microstructure, but were susceptible to large systematic errors in stress distribution estimation (Fig. 10). Current two-dimensional map methods provide direct measurements of the stress distribution, but may not investigate a large-enough area of the microstructure to provide an adequate average (Fig. 5). The current work goes some way to overcoming these issues: Future two-dimensional mapping work needs to obtain enough data to achieve adequate precision through microstructural averaging and future integrated scan work should use the two-peak approach to achieve accurate stress estimation. In addition, models and observations of kinetics of stress development as a function of grain size [10,19], of equilibrium distributions of stress [10,20], and of fracture [21] can now be tested using a range of fluorescence measurements, and this will be the subject of future work.

References

[1] R.D. Munro, Evaluated material properties for a sintered α-alumina, J. Am. Ceram. Soc. 80 (1997) 1919–1928.
[2] S. Galal Yousef, J. Rödel, E.R. Fuller Jr., A. Zimmermann, B.S. El-Dasher, Microcrack evolution in alumina ceramics: experiment and simulation, J. Am. Ceram. Soc. 88 (2005) 2809–2816.
[3] S.J. Bennison, B.R. Lawn, Role of interfacial grain-bridging sliding friction in the crack-resistance and strength properties of nontransforming ceramics, Acta Metall 37 (1989) 2659–2671.
[4] G.A. Myers, C.A. Michaels, R.F. Cook, Quantitative mapping of stress heterogeneity in polycrystalline alumina using hyperspectral fluorescence microscopy, Acta Mater 106 (2016) 272–282.
[5] R.F. Cook, C.A. Michaels, Review: coefficients for stress, temperature, and composition effects in fluorescence measurements of alumina, J. Res. Natl Inst. Stan. 122 (2017) 1–26.
[6] R.H. Dauskardt, J.W. Ager III, Quantitative stress mapping in alumina composites by optical fluorescence imaging, Acta Mater. 44 (1996) 625–641.
[7] M.C. Teague, T. Rodgers, S. Grutzik, S. Meserole, Characterization and modeling of microstructural stresses in alumina, J. Am. Ceram. Soc. 101 (2018) 2155–2161.
[8] C.A. Michaels, R.F. Cook, Determination of residual stress distributions in polycrystalline alumina using fluorescence microscopy, Mater. Des. 107 (2016) 478–490.
[9] Q. Ma, D.R. Clarke, Stress measurement in single-crystal and polycrystalline ceramics using their optical fluorescence, J. Am. Ceram. Soc. 76 (1993) 1433–1440.
[10] Q. Ma, D.R. Clarke, Piezospectroscopic determination of residual stresses in polycrystalline alumina, J. Am. Ceram. Soc. 77 (1994) 298–302.
[11] V. Sergo, G. Pezzotti, O. Sbaizero, T. Nishida, Grain size influence on residual stresses on alumina/zirconia composites, Acta Mater 46 (1998) 1701–1710.
[12] K. Dassios, C. Galiotis, Fluorescence studies of polycrystalline Al_2O_3 composite constituents: piezo-spectroscopic calibration and applications, Appl. Phys. A 79 (2004) 647–659.
[13] L. Grabner, Spectroscopic technique for the measurement of residual stress in sintered Al_2O_3, J. Appl. Phys. 49 (1978) 580–583.
[14] R.F. Cook, E.G. Liniger, R.W. Steinbrech, F. Deuerler, Sigmoidal indentation-strength characteristics of polycrystalline alumina, J. Am. Ceram. Soc. 77

(1994) 303–314.
[15] J. He, D.R. Clarke, Polarization dependence of the Cr^{3+} R-Line fluorescence from sapphire and its application to crystal orientation and piezospectroscopic measurement, J. Am. Ceram. Soc. 80 (1997) 69–78.
[16] S.H. Margueron, D.R. Clarke, The use of polarization in the piezospectroscopic determination of the residual stresses in polycrystalline alumina films, Acta Mater. 54 (2006) 5551–5557.
[17] A. Zimmermann, E.R. Fuller Jr., J. Rödel, Residual stress distributions in ceramics, J. Am. Ceram. Soc. 82 (1999) 5155–5160.
[18] V.R. Vedula, S.J. Glass, D.M. Saylor, G.S. Rohrer, W.C. Carter, S.A. Langer, E.R. Fuller Jr., Residual-stress predictions in polycrystalline alumina, J. Am. Ceram. Soc. 84 (2001) 2947–2954.
[19] J.E. Blendell, R.L. Coble, Measurement of stress due to thermal expansion anisotropy in Al_2O_3, J. Am. Ceram. Soc. 65 (1982) 174–178.
[20] W. Kreher, A. Molinari, Residual stresses in polycrystals as influenced by grain shape and texture, J. Mech. Phys. Solid. 41 (1993) 1955–1977.
[21] D.R. Clarke, Microfracture in brittle solids resulting from anisotropic shape changes, Acta Metall. 28 (1980) 913–924.